Numerical Simulation of Particle Behavior in a Bifurcated Channel with Asymmetric Flow Distribution

DAISUKE HARAGUCHI[1], TOMOHIRO FUKUI[2,*]
[1]Department of Master's Program of Mechanophysics,
Kyoto Institute of Technology,
Matsugasaki Goshokaido-cho, Sakyo-ku, Kyoto 606-8585,
JAPAN

[2]Department of Mechanical Engineering,
Kyoto Institute of Technology,
Matsugasaki Goshokaido-cho, Sakyo-ku, Kyoto 606-8585,
JAPAN

**Corresponding Author*

Abstract: - In recent years, inhalation therapy has become the standard treatment for chronic obstructive pulmonary disease (COPD). To enhance the effect of inhalation therapy, the effective deposition of drug particles into the affected area is required. Numerous simulations have been conducted on particle deposition within the airways of the lung. A one-way coupling scheme is often used in computational methods to reduce computational costs; however, to consider the effect of finite particle sizes, a two-way coupling scheme is required. This scheme includes both fluid-particle interactions and considers the Magnus effect, Saffman lift, and wall effect. By taking lift forces into account, particle migration in the direction perpendicular to the flow may be captured. In this study, we examined the flow and particle distribution at bifurcations using a two-way coupling scheme, particularly in environments where the inertial effects acting on particles cannot be neglected. A two-dimensional symmetric bifurcated channel was used as the calculation model. The regularized lattice Boltzmann method was applied as the governing equation for the flow field and the virtual flux method was used to represent the two-dimensional bifurcated channels and particles. A flow field characterized by an asymmetric flow distribution was reproduced and the particle behavior within this field was evaluated. The results indicated that because of particle migration, the particle crossed the boundary line that divides the flow rate distribution between the two bifurcated channels. This suggests that discrepancies may occur between flow and particle distribution at the bifurcation in environments where inertial effects cannot be neglected.

Key-Words: - COPD, Inhalation therapy, Two-way coupling scheme, Migration, Lattice Boltzmann method, Particle behavior, Asymmetry flow distribution.

Received: August 11, 2024. Revised: December 15, 2024. Accepted: February 13, 2025. Published: April 2, 2025.

1 Introduction

Chronic obstructive pulmonary disease, commonly known as COPD, was the fourth leading cause of death worldwide in 2021 according to the WHO, [1]. COPD is a disease that causes inflammation in the lungs and decreased lung function resulting from long-term inhalation and exposure to harmful substances, such as tobacco smoke.

Inhalation therapy is currently the standard treatment for COPD. This therapy delivers particulate drugs through oral inhalation. To enhance its effects, the effective deposition of drug particles to the affected area is required. In addition, it is necessary to determine the behavior of particles in the pulmonary airways to understand the deposition pattern of particles in the airways.

Numerous studies have employed numerical simulations to analyze airflow dynamics and particle deposition within the lung airways, with some also utilizing AI-based approaches in respiratory research, [2], [3].

In simulations, the airways form two branches from the bronchi, and they undergo approximately 23 bifurcations before they reach the alveoli. This geometrically complex structure results in high computational costs, which pose a major challenge. Therefore, most previous studies have used simple models to study these processes. A simplified model

was developed to examine particle deposition, assuming that the bronchi branch regularly from the 3rd to the 17th generation, with one daughter branch severed at each bifurcation, [4].

The symmetric two-branching model proposed by Weibel has been used in many simulations because of its simplicity, [5]. A three-dimensional symmetric model based on the Weibel model was created, with a stenosis added to part of the structure to examine particle deposition, [6]. A model with symmetric branching from the 3rd to the 10th generation was used, where one daughter branch was severed at each bifurcation to simulate particle behavior, [7].

In addition to the simplified models mentioned above, many studies have used a one-way coupling scheme, which considers only the effects of the fluid on the particles to reduce computational costs, [8], [9], [10], [11], [12]. In a one-way coupling scheme, it is primarily assumed that only drag acts on the particles, whereas lift forces are neglected. In simulations using a one-way coupling scheme, particle motion is fixed along streamlines. Therefore, when focusing on particle behavior at bronchial bifurcations, the microscopic particle distribution ratio at the bifurcation is determined by the macroscopic flow rate distribution ratio. However, in numerical simulations of particle behavior within the lung airways, the computational domain is located within the boundary layer. Therefore it is necessary to consider the lift forces acting on the particles.

To account for the lift force acting on the particles, it is necessary to use a two-way coupling scheme that considers fluid-particle interactions. A two-way coupling scheme can take the Magnus effect, Saffman lift, and wall effect into consideration. A distinctive feature of the two-way coupling scheme is that it considers the rotational motion and size of the particles; however, it requires high resolution, leading to higher computational costs compared with a one-way coupling scheme. To clarify the detailed particle behavior within the pulmonary airways, it is necessary to apply the two-way coupling scheme to the entire region; however, this approach is challenging because of its high computational cost.

Therefore, in this study, regions where inertial effects cannot be neglected were locally extracted and investigated. It has been reported that the inertial effects acting on particles must be considered when the particle Reynolds number in the flow exceeds 1.0×10^{-3}, [13]. In the pulmonary airway, an environment where the particle Reynolds number exceeds 1.0×10^{-3} emerges in the 4th to 10th bronchial generations. This suggests that inertial effects must be considered. By appropriately selecting between the one-way coupling scheme and the two-way coupling scheme based on the mechanical environment, it is possible to achieve high-accuracy simulations while keeping computational costs low.

In the pulmonary airway, the value of Re_p does not exceed 1.0×10^{-3} in the early bronchial generations (0th to 3rd generations), and this indicates that the one-way coupling scheme can provide sufficient accuracy. However, as mentioned above, as bifurcations are passed and the central region (4th to 10th generations) is approached, the particle Reynolds number increases, and environments where it exceeds 1.0×10^{-3} emerge.

In such environments, the one-way coupling scheme may not provide sufficient accuracy, and to achieve more precise analysis, the application of the two-way coupling scheme is necessary. However, at present, research using multi-generation models primarily applies the one-way coupling scheme, and studies utilizing the two-way coupling scheme have not been conducted. Therefore, in this study, regions where inertial effects cannot be neglected are extracted, and calculations are performed by applying the two-way coupling scheme. Additionally, this study focused on a localized bifurcation in the pulmonary airways to examine microscopic particle behavior.

In addition, when considering the lift forces acting on particles at bifurcations, the particles may deviate from the streamlines. One phenomenon in which particles deviate from streamlines is the Segre–Silberberg effect, [14]. This occurs when particles flowing through a tube under the influence of inertia migrate perpendicular to the flow and aggregate at specific radial equilibrium positions. During circular Poiseuille flow, particles aggregate at a position approximately 0.6 times the tube radius. This equilibrium position is determined by the balance between the wall effect and the lift force, which is caused by the shear gradient of the flow field, [15]. This suggests that in bronchial bifurcations within the lung airways, particles in the parent branch migrate across the flow distribution boundary before the bifurcation. As a result, discrepancies may occur between macroscopic flow distribution and microscopic particle distribution. In this study, we examined the flow and particle distribution at a bifurcation using a two-way coupling scheme. The flow distribution boundary line described above refers to the line that determines whether the fluid flows into either of the two branches. In a symmetric bifurcated channel,

when flow distribution is symmetric, this boundary line is the centerline of the channel. In this study, we reproduced a flow field in which the flow distribution was asymmetric and examined the particle behavior at the bifurcation in an environment, in which the boundary line did not coincide with the channel centerline.

2 Methods

2.1 Computational Models

The two-dimensional bifurcated channel shown in Figure 1 was used to examine particle behavior at the bifurcation.

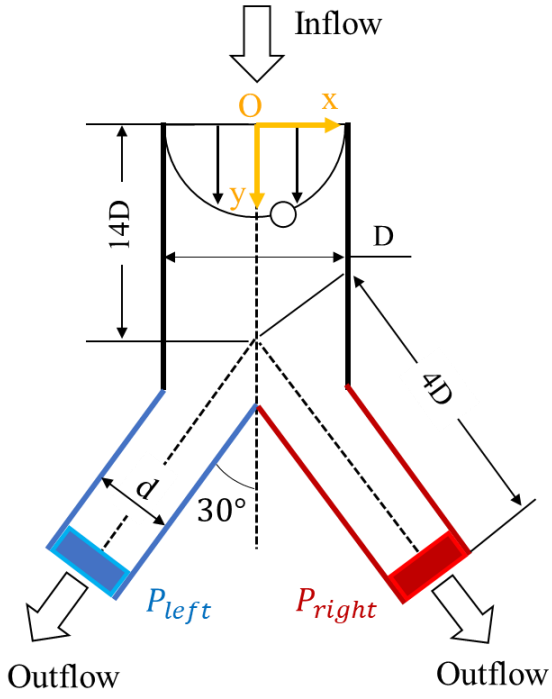

Fig. 1: Schematic diagram of the two-dimensional bifurcated channel

The channel width was set as the characteristic length D, the left wall of the parent branch was $-0.5D$, the center was $0.0D$, and the right wall of the parent branch was $0.5D$. The channel diameter d of the left and right daughter branches after bifurcation was set to $d = D/2$ and the bifurcation angle was set to 30° for both the left and right sides. Air was considered the working fluid. The characteristic length was set to $D = 0.001$ m, the characteristic velocity was set to $U = 0.96$ m/s, and the kinematic viscosity was set to $\nu = 15.01 \times 10^{-6}$ m^2/s. The Reynolds number was set to $Re = 64$ and calculated as UD/ν. In addition, the simulation time was 0.012 s. The confinement C, defined as the ratio of the particle diameter r to the channel width D, was set to $C = r/D = 0.1$. The particle Reynolds number Re_p is given by $Re_p = Re \times C^2 = 0.64$. The behavior of particles in the flow channel can be systematically discussed based on the particle Reynolds number. Therefore, in this study, based on the similarity law, the particle Reynolds number used in the calculations was set to the order of 10^{-1}, which corresponds to the order of the particle Reynolds number in the bronchial generations 4 to 10 during inhalation. Additionally, from the perspective of computational cost, the Reynolds number was set lower and the confinement higher than in the actual environment. Previous numerical simulation studies confirmed that particles migrated to the equilibrium position when the Reynolds number reached 32 and 64, and their results suggested that the lift force acting on the particles could not be neglected, [16]. In this previous study, the confinement ratio was set to 0.05. From the perspective of the particle Reynolds number, it is considered that the effect of lift cannot be neglected when the particle Reynolds number reaches 0.08 or 0.16. In this study, the particle Reynolds number was set to 0.64. Therefore, the application of the two-way coupling scheme is considered necessary. At the inlet boundary, Poiseuille flow was imposed, whereas a Neumann boundary condition, $\partial P/\partial \boldsymbol{n} = 0$, was applied for the pressure. At the outlet boundary, a Neumann boundary condition, $\partial \boldsymbol{u}/\partial \boldsymbol{n} = \boldsymbol{0}$, was applied for the velocity, whereas a Dirichlet boundary condition was imposed for the pressure. In addition, a no-slip condition was applied to the wall surface. In many simulations of the pulmonary airway, a uniform flow or Poiseuille flow is introduced at the inlet, and a Dirichlet boundary condition is applied to the outlet pressure. This approach is commonly used and is considered a standard boundary condition setting. Additionally, in this calculation, we focused on the particle behavior at the bifurcation. Since the analysis area is sufficiently distant from the boundaries, the boundary conditions are considered not to affect particle behavior.

2.2 Governing Equations

In this study, the regularized lattice Boltzmann method (2D9V model), an improved version of the lattice Boltzmann method, was used as the governing equation for the fluid. This method retains the advantages of the lattice Boltzmann method, including the high computational efficiency and algorithmic simplicity, while reducing memory usage and improving computational stability. In the

lattice Boltzmann method, several particle distribution models have been proposed. In this study, the two-dimensional nine-velocity (2D9V) model was adopted. In the 2D9V model, the discrete velocities of particles are given by the following three equations.

$$e_\alpha = \begin{cases} c(0,0) & (\alpha = 0) \\ c\left(\cos\frac{(\alpha-1)\pi}{2}, \sin\frac{(\alpha-1)\pi}{2}\right) & (\alpha = 1-4) \\ \sqrt{2}c\left(\cos\frac{(2\alpha-9)\pi}{2}, \sin\frac{(2\alpha-9)\pi}{2}\right) & (\alpha = 5-8) \end{cases} \quad (1)$$

Here, c represents the advection velocity of particles and is defined as $c = \delta x/\delta t$ using the time step δt and the spatial grid size δx.

In this study, a single-relaxation-time model based on the BGK approximation, which simplifies the collision operator, was applied to the governing equations for fluid analysis. The distribution function f_α, which represents the presence of particles with discrete velocity e_α, satisfies the discrete velocity Boltzmann equation, as shown in Equation (2).

$$\frac{\partial f_\alpha}{\partial t} + e_\alpha \frac{\partial f_\alpha}{\partial x} = \frac{1}{\tau}\left(f_\alpha^{eq} - f_\alpha\right) \quad (2)$$

τ represent the relaxation time, where the left-hand side of Equation (2) corresponds to the advection term, and the right-hand side represents the collision term. When a specific discretization is applied to Equation (2), the following equation is obtained.

$$\begin{aligned} f_\alpha(t+\delta t, x+e_\alpha\delta t) &= f_\alpha(t,x) \\ &+ \frac{1}{\tau}\left(f_\alpha^{eq}(t,x) - f_\alpha(t,x)\right) \end{aligned} \quad (3)$$

Here, $f_\alpha(t,x)$ and $f_\alpha^{eq}(t,x)$ represent the particle distribution function and the equilibrium distribution function, respectively, which correspond to the discrete velocity vector e_α at position x on the lattice at time t. τ represents the relaxation time, and by applying the Chapman-Enskog expansion to Equation (3) so that it satisfies the Navier-Stokes equations, it can be expressed as shown in Equation (4).

$$\tau = \frac{3\nu}{c\delta x} + \frac{1}{2} \quad (4)$$

Here, ν represents the kinematic viscosity. Additionally, the equilibrium distribution function f_α^{eq} is obtained by performing a Taylor expansion of Maxwell's equilibrium distribution function with respect to velocity and neglecting terms of third order and higher, as expressed in the following equation.

$$f_\alpha^{eq} = \omega_\alpha \rho \left\{1 + \frac{3(e_\alpha \cdot u)}{c^2} + \frac{3(e_\alpha \cdot u)^2}{2c^4} - \frac{3u^2}{2c^2}\right\} \quad (5)$$

Here, ρ represents the fluid density, and u denotes the velocity vector. The weighting function ω_α in the 2D9V model is given by the following three equations.

$$\omega_\alpha \begin{cases} 4/9 & (\alpha = 0) \\ 1/9 & (\alpha = 1-4) \\ 1/36 & (\alpha = 5-8) \end{cases} \quad (6)$$

The distribution function obtained through the above process is used to calculate the macroscopic physical quantities, namely the density ρ and the momentum ρu, as follows.

$$\rho = \sum_\alpha f_\alpha \quad (7)$$

$$\rho u = \sum_\alpha e_\alpha f_\alpha \quad (8)$$

In the regularized lattice Boltzmann method, the distribution function f_α is expressed using the stress tensor Π_{ij} as shown in Equation (9).

$$\Pi_{ij}(t,\boldsymbol{x}) = \sum_\alpha e_{\alpha i} e_{\alpha j} f_\alpha(t,\boldsymbol{x}) \quad (9)$$

The nonequilibrium components of the stress tensor Π_{ij}^{neq} and the nonequilibrium part of the distribution function f_α are expressed as follows:

$$\Pi_{ij}^{neq}(t,\boldsymbol{x}) = \Pi_{ij}(t,\boldsymbol{x}) - \Pi_{ij}^{eq}(t,\boldsymbol{x}) \quad (10)$$

$$f_\alpha^{neq}(t,\boldsymbol{x}) = f_\alpha(t,\boldsymbol{x}) - f_\alpha^{eq}(t,\boldsymbol{x}) \quad (11)$$

By applying the Chapman-Enskog expansion, the nonequilibrium part of the distribution function can be expressed as shown in Equation (12). At this stage, only the first-order term is used as an assumption.

$$f_\alpha^{neq}(t,\boldsymbol{x}) \cong f_\alpha^1(t,\boldsymbol{x}) = -\frac{\delta t}{c_s^2}\tau\omega_\alpha Q_{\alpha ij}\partial_i \rho u_j \quad (12)$$

where $Q_{\alpha ij}$ is the regularized tensor defined as $Q_{\alpha ij} = e_{\alpha i}e_{\alpha j} - c_s^2\delta_{ij}$. Using Equations (9) and (10), the nonequilibrium component of the stress tensor can be expressed as follows:

$$\Pi_{ij}^{neq}(t,\boldsymbol{x}) \cong \sum_{\alpha} e_{\alpha i}e_{\alpha j}f_{\alpha}^{1}(t,\boldsymbol{x}) = -\delta t c_s^2 \tau\left(\partial_i \rho u_j + \partial_j \rho u_i\right) \tag{13}$$

Here, using Equations (12) and (13), $f_{\alpha}^{1}(t,\boldsymbol{x})$ can be expressed as shown in Equation (14).

$$f_{\alpha}^{1}(t,\boldsymbol{x}) = \frac{\omega_{\alpha}}{2c_s^4}Q_{\alpha ij}\Pi_{ij}^{neq}(t,\boldsymbol{x}) \tag{14}$$

The time evolution equation in the regularized lattice Boltzmann method are expressed as shown in Equation (15) using Equations (11), (12), and (14).

$$f_{\alpha}(t+\delta t, \boldsymbol{x}+\boldsymbol{e}_{\alpha}\delta t) = f_{\alpha}^{eq}(t,\boldsymbol{x}) + \left(1-\frac{1}{\tau}\right)f_{\alpha}^{1}(t,\boldsymbol{x}) \tag{15}$$

In this study, to reduce errors caused by compressibility, the incompressible formulation using the pressure distribution function was adopted, as employed in a previous study, [17]. According to this previous study, when the initial density is denoted as ρ_0 and the small variation in density as $\Delta\rho$, the total density can be decomposed as $\rho = \rho_0 + \Delta\rho$. In an incompressible flow field, $\Delta\rho$ can be considered negligible as a small quantity. Consequently, a relationship between the pressure distribution function and the density distribution function can be derived as follows.

$$p_{\alpha} = c_s^2 f_{\alpha} \tag{16}$$

Thus, the time evolution equation formulated for incompressible flow is given as follows.

$$p_{\alpha}(t+\delta t, \boldsymbol{x}+\boldsymbol{e}_{\alpha}\delta t) = p_{\alpha}^{eq}(t,\boldsymbol{x}) + \left(1-\frac{1}{\tau}\right)p_{\alpha}^{1}(t,\boldsymbol{x}) \tag{17}$$

2.3 Governing Equation for Particles

A two-way coupling scheme may be used to take into account the lift forces acting on the particles as well as the translational and rotational motions of the circular particles. Newton's second law is used for the equation of motion for translation and the angular equation of motion is used for the equation of motion for rotation, which are expressed by Equations (18) and (19), respectively, as follows:

$$m_p\frac{d^2\boldsymbol{x}_p}{dt^2} = \boldsymbol{F}_p \tag{18}$$

$$I\frac{d^2\theta_p}{dt^2} = T_p \tag{19}$$

where m_p is the mass of the particle, $\boldsymbol{x}_p$ is the position vector of the particle, $\boldsymbol{F}_p$ is the external force vector acting on the particle, I is the moment of inertia, θ_p is the rotational angle of the particle, and T_p is the torque applied to the particle.

In this study, we focused on three components of lift forces: the Magnus effect-induced lift, the Saffman lift, and the wall effect. These three lift forces are obtained as a combined value from the fluid force. The external force vector acting on the particle, $\boldsymbol{F}_{\mathrm{p}} = (F_{\mathrm{p}x}, F_{\mathrm{p}y})$, was calculated from the fluid force around the particle as follows.

$$F_{\mathrm{p}x} = \int_c \left(p_{\mathrm{p}} - p_0\right)\cos\theta\, ds + \int_c \tau_{\mathrm{p}}\sin\theta\, ds \tag{20}$$

$$F_{\mathrm{p}y} = -\int_c \left(p_{\mathrm{p}} - p_0\right)\sin\theta\, ds + \int_c \tau_{\mathrm{p}}\cos\theta\, ds \tag{21}$$

Here, the vertical component of the external force vector acting on the particle, $F_{\mathrm{p}y}$ is calculated as the lift force. Additionally, p_{p} and p_0 represent the pressure acting on the particle surface and the reference pressure, respectively, and τ_{p} represents the shear stress acting on the particle surface.

The Equations of motion (18) and (19) are discretized employing the third-order Adams-Bashforth scheme and the numerical computations are carried out based on these Equations. The discretized equations are shown as (22), (23), (24), and (25).

$$\dot{\boldsymbol{x}}_p^{n+1} = \dot{\boldsymbol{x}}_p^{n} + \Delta t\frac{23\boldsymbol{F}_p^{n} - 16\boldsymbol{F}_p^{n-1} + 5\boldsymbol{F}_p^{n-2}}{12m_p} \tag{22}$$

$$\boldsymbol{x}_p^{n+1} = \boldsymbol{x}_p^{n} + \Delta t\frac{5\dot{\boldsymbol{x}}_p^{n+1} + 8\dot{\boldsymbol{x}}_p^{n} - \dot{\boldsymbol{x}}_p^{n-1}}{12} \tag{23}$$

$$\dot{\theta}_p^{n+1} = \dot{\theta}_p^n + \Delta t \frac{23T_p^n - 16T_p^{n-1} + 5T_p^{n-2}}{12I} \quad (24)$$

$$\theta_p^{n+1} = \theta_p^n + \Delta t \frac{5\dot{\theta}_p^{n+1} + 8\dot{\theta}_p^n - \dot{\theta}_p^{n-1}}{12} \quad (25)$$

2.4 Virtual Flux Method

The virtual flux method was used to represent and compute the bifurcated channel and circular particles on a Cartesian grid, [18]. A schematic view of the virtual flux method is shown in Figure 2.

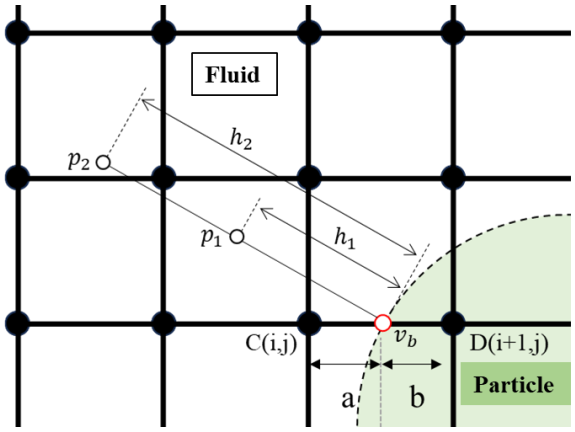

Fig. 2: Schematic view of the virtual flux method. The white-shaded area represents the fluid region, the green-shaded area represents the circular particle, and the red circles indicate the virtual boundary points

The flow around a fixed two-dimensional circular cylinder was analyzed using both VFM and IBM, and the two methods were compared, [19]. As a result, it was reported that compared to IBM, VFM could capture physical quantities near the boundary more sharply. Additionally, it was reported that in VFM, the convergence rate could be improved by adjusting the interpolation accuracy of pressure according to the distance between objects.

This method is easy to implement because it only requires the addition of a calculation routine for the virtual flux method into a standard flow simulation program.

A no-slip condition was applied to the velocity as the boundary condition for the

bifurcated channel and the surface of circular particles. For pressure, an approximate boundary condition with a zero normal pressure gradient was applied. The respective equations are as follows:

$$\boldsymbol{u}_{vb} = \boldsymbol{u}_{wall} \quad (26)$$

$$\frac{\partial p}{\partial \boldsymbol{n}} = 0 \quad (27)$$

As an example, we considered a flow field separated into fluid and circular particles as illustrated in Figure 2. When we calculated the distribution function at lattice point C for the next time step, we focused on the case in which the distribution function at lattice point D crossed the virtual boundary and moved to lattice point C. In this case, the distribution function at lattice point D cannot pass through the virtual boundary. Instead, the virtual distribution function at lattice point D is determined using the distribution function at the virtual boundary point v_b. As a result, the distribution function at lattice point D can be obtained solely from the physical quantities in the fluid region. The equilibrium pressure distribution function $p_\alpha^{eq}(t, \boldsymbol{x}_{vb})$ at the virtual boundary point is shown in Equation (28).

$$p_\alpha^{eq}(t, \boldsymbol{x}_{vb}) = \omega_\alpha \left[p_{vb} + \rho_0 \left\{ (\boldsymbol{e}_\alpha \cdot \boldsymbol{u}_{vb}) + \frac{3}{2}\frac{(\boldsymbol{e}_\alpha \cdot \boldsymbol{u}_{vb})^2}{c^2} - \frac{1}{2}\boldsymbol{u}_{vb}^2 \right\} \right] \quad (28)$$

where p_{vb} is the pressure at the virtual boundary point and where Equation (27) is approximated with second-order accuracy. Using the pressures p_1, p_2 at points h_1, $h_2$away from the virtual boundary point v_b in the normal direction, p_{vb} is expressed as shown in Equation (29).

$$p_{vb} = \frac{h_1^2 p_2 - h_2^2 p_1}{h_2^2 - h_1^2} \quad (29)$$

Here, the pressures ($p1$, $p2$) are calculated by weighting the pressures at the four surrounding lattice points using only the values in the fluid region. For this purpose, $h_1 = \sqrt{2}$, $h_2 = 2\sqrt{2}$ were applied. The virtual equilibrium pressure distribution function at lattice point D was obtained through linear extrapolation using the internal division ratios a and b along line segment CD. Interpolation was applied to make the nonequilibrium components of the pressure distribution function at lattice point C and point D equal.

$$p_\alpha^{eq^*}(t, \boldsymbol{x}_D) = -\frac{b}{a} p_\alpha^{eq}(t, \boldsymbol{x}_C) + \frac{a+b}{a} p_\alpha^{eq}(t, \boldsymbol{x}_{vb}) \quad (30)$$

$$p_\alpha^{neq^*}(t, \boldsymbol{x}_D) = p_\alpha^{neq}(t, \boldsymbol{x}_C) \quad (31)$$

From the above equations, the distribution function at lattice point C was calculated using the virtual equilibrium distribution function $p_\alpha^{eq^*}(t, \boldsymbol{x}_D)$ and the nonequilibrium component $p_\alpha^{neq^*}(t, \boldsymbol{x}_D)$at lattice point D. This was achieved through the time evolution equation (32).

$$p_\alpha(t + \delta t, \boldsymbol{x} + \boldsymbol{e}_\alpha \delta t) = p_\alpha^{eq}(t, \boldsymbol{x}_D) + \left(1 - \frac{1}{\tau}\right) p_\alpha^{neq^*}(t, \boldsymbol{x}_D) \quad (32)$$

3 Validation

3.1 Computational Model and Conditions

In pipe flow, it was known that particles flowing with inertia accumulate at specific equilibrium positions. Such an aggregation phenomenon is known as the Segré-Silberberg effect. In this validation, we investigate particle behavior under three different conditions. In Condition 1, particles were released from different initial positions to confirm the Segré-Silberberg effect. In Conditions 2 and 3, the Reynolds number and confinement, respectively, were varied to examine their influence on the equilibrium position. By comparing the results with previous studies, this validated its physical accuracy. A two-dimensional parallel-plate channel was used as the computational model for the validation, as shown in Figure 3. The computational conditions were listed in Table 1 (Appendix) and the parameters that were varied in each condition were presented in Table 2 (Appendix).

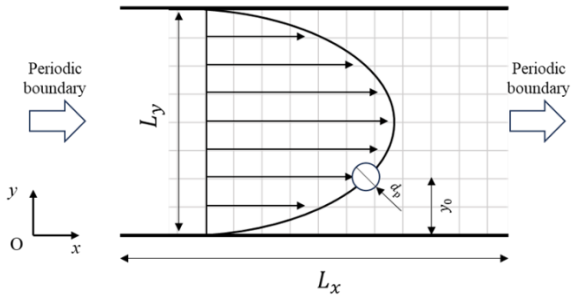

Fig. 3: Schematic diagram of a single circular particle in a two-dimensional channel

3.2 Computational Results

The particle trajectories in Condition 1 were shown in Figure 4. In Condition 1, particles were released from three different initial positions: $y_0 = 0.20, 0.30, 0.40$. From Figure 4, it was confirmed that particles released from different initial positions reached the same equilibrium position. This result suggests that the Segré-Silberberg effect was observed. Next, the particle trajectories in Condition 2 were shown in Figure 5. In Condition 2, particles were released at three different Reynolds numbers: $Re = 12.73, 27.54, 54.91$. The initial particle position was set to $y_0 = 0.40$.

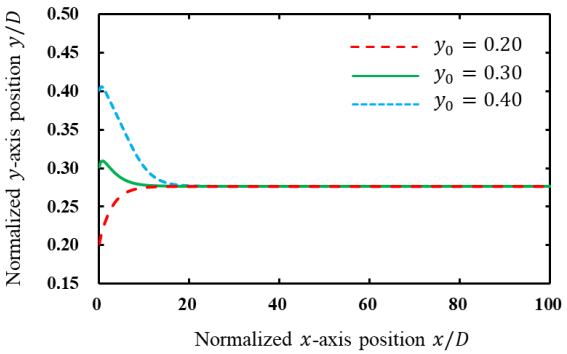

Fig. 4: Particle trajectories with different initial position

Additionally, the particle equilibrium positions were presented in Table 3 along with the results from previous studies.

Table 3. Equilibrium position of the center of the particle at different Reynolds number

Re	Present	Inamuro
12.73	0.2786	0.2745
27.54	0.2766	0.2733
54.91	0.2759	0.2723

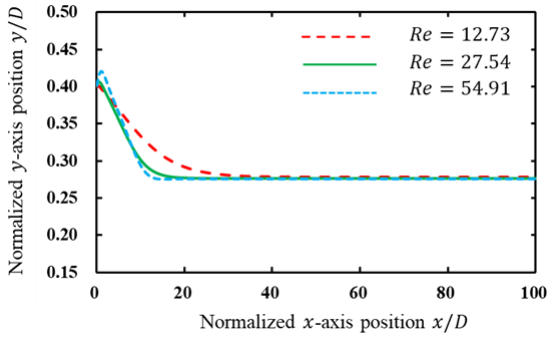

Fig. 5: Particle trajectories at different Reynolds numbers

From Figure 5, it was observed that as the Reynolds number increased, the distance required to reach the equilibrium position became shorter.

Additionally, from Table 3, it was found that the equilibrium position shifted closer to the wall. This trend is consistent with previous results, indicating the validity of the present study, [20].

Next, the particle trajectories in Condition 3 were shown in Figure 6. In Condition 3, particles were released at three different confinement values: $C = 0.20, 0.25, 0.30$. The initial particle position was set to $y_0 = 0.40$, and the Reynolds number was set to $Re = 27.54$. This trend is consistent with the findings of [20].

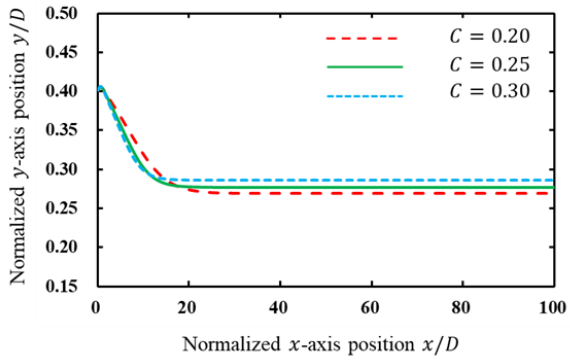

Fig. 6: Particle trajectories at different confinement.

Through numerical analysis under the three conditions and comparison with previous studies, this validated its physical accuracy. Additionally, the equilibrium position can be summarized by the particle Reynolds number, $Re_P = Re \times C^2$. Based on the above computational results, while the equilibrium position varies with Re_P, it is generally located at approximately 60% of the channel radius.

3.3 Verification

In this study, a grid resolution verification was conducted using a two-dimensional parallel-plate channel to investigate the minimum number of grid points assigned to a particle without losing numerical reliability. The computational model was the same as that shown in Figure 3. The computational conditions were listed in Table 4 (Appendix). In a single-particle flow, the number of grid points assigned to the particle diameter was set to 10, 15, 20, and 25 cells, and the equilibrium position of the particle was investigated. The relationship between the number of grid points assigned to the particle diameter and the equilibrium position was shown in Figure 7.

From Figure 7, it was shown that as the number of grid points assigned to the particle increased, the equilibrium position converged. Additionally, at grid numbers of 20 and 25, the difference in equilibrium position values was minimal. From this, the number of grid points assigned to the particle was set to 20 cells for subsequent particle behavior analysis. This corresponds to the white-filled point in Figure 7.

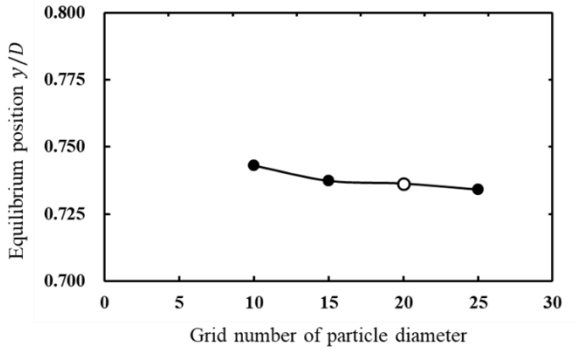

Fig. 7: Particle trajectories at different confinement

4 Result and Discussion

4.1 Particle Behavior in a Symmetric Flow Field

To examine particle behavior in an asymmetric flow field, we first examined it as a test case in a flow field, in which the outlet pressures were equal on both sides and the flow distribution was symmetric. The initial positions of the particles on the left and right were $(-0.2, 1.0)$ and $(0.2, 1.0)$ for normalized coordinates $(x/D, y/D)$ respectively, and the Reynolds number was set to $Re = 64$. The calculated particle trajectories are shown in Figure 8 (Appendix). In this test case, the flow distribution was symmetric, so the boundary line dividing the flow was the centerline of the channel. The fluid on the left side of the centerline flows into the left daughter branch after the bifurcation, whereas the fluid on the right side flows into the right daughter branch.

As shown in Figure 8 (Appendix), when particles are positioned to the left of the channel centerline, they flow into the left branch after the bifurcation. Similarly, particles positioned to the right of the centerline flow into the right branch.

Figure 9 (Appendix) shows the extracted particle trajectory within the parent branch region from Figure 8 (Appendix). In Figure 9 (Appendix), the horizontal axis corresponds to $x = -0.5$ for the left wall of the parent branch, $x = 0.0$ for the channel centerline, and $x = 0.5$ for the right wall of the parent branch.

From Figure 9(a) (Appendix), particle migration toward the left wall is apparent, whereas Figure 9(b) (Appendix) shows migration toward the right wall.

For the particle flow between two-dimensional parallel plates, the mechanical equilibrium positions of the particle at $Re = 64$ and confinement $C = 0.1$ are located at $x/D = -0.23$ and $x/D = 0.23$. These positions are symmetric about the y-axis. Therefore, the particle in Figure 9(a) (Appendix) is considered to migrate to the position $x/D = -0.23$, whereas the particle in Figure 9(b) (Appendix) migrates to the position $x/D = 0.23$. This suggests that in a symmetric flow field, particles migrate away from the channel centerline, which serves as the flow distribution boundary. Therefore, it is unlikely that flow and particle distribution differ.

4.2 Particle Behavior in an Asymmetric Flow Field

In this study, we examined particle behavior under conditions in which a pressure difference was applied to the left and right outlets. This pressure difference caused the flow distribution to become asymmetric. The pressure difference between the left and right outlets was defined as ΔP, with $P_{left} = P_{right} + \Delta P$. In addition, ΔP was set to 3.34 Pa. Under these conditions, the left-to-right flow distribution ratio was $69:31$ when the inlet flow rate was set to 100. Figure 10 shows the velocity distributions at three cross-sections near the bifurcation in the parent branch located at $y = 12D, 14D$, and $14.25D$. Figure 11 (Appendix) shows the relationship between the outlet pressure difference ΔP^*, the x/D coordinates of the flow distribution boundary line, and the mechanical equilibrium position within the parent branch region. ΔP^* represents the pressure difference normalized by $1/2 \times \rho U^2$, which corresponds to the dynamic pressure.

In this study, a geometrically symmetric model was used, and the velocity distribution peak was reproduced at approximately 0.5 times the channel radius by adjusting the pressure difference at the outlet boundary condition. The boundary line that determines which daughter branch the fluid enters was located at 0.13, as shown in Figure 11(b) (Appendix). This position varied with changes in the pressure difference, as illustrated in Figure 11(a) (Appendix).

From Figure 10, it is apparent that the velocity distribution becomes eccentric as the flow approaches the bifurcation. In addition, at the cross-section $y = 12D$, the velocity distribution shows a parabolic shape, which confirms that it is Poiseuille flow. Therefore, at $y = 12D$, the mechanical equilibrium position of the particles is considered to be located at approximately 0.6 times the tube radius. The flow rate error before and after the bifurcation was 0.09%, which indicates that the law of conservation of mass is satisfied.

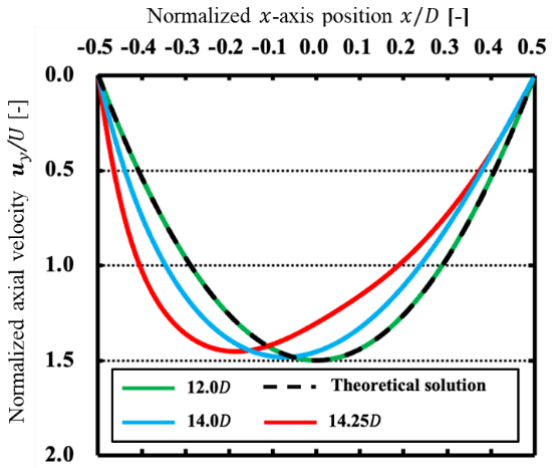

Fig. 10: Velocity profile within the parent branch

From Figure 11(a) (Appendix), it is evident that as the normalized pressure difference ΔP^*increases, the boundary line approaches the right wall of the parent branch. As shown in Figure 11(b) (Appendix), when the boundary line is located closer to the center of the channel than the equilibrium position and the particles are positioned between the channel center and the boundary line (the gray region in Figure 11(b) (Appendix)), the particles may cross the boundary line as they migrate toward the equilibrium position. We set the normalized outlet pressure difference to $\Delta P^* = 6.00$ which corresponds to the dimensionless value of 3.34 Pa when normalized by dynamic pressure, as indicated by the red circle in Figure 11(b) (Appendix). We placed the initial position of the particle within the gray region and examined particle behavior.

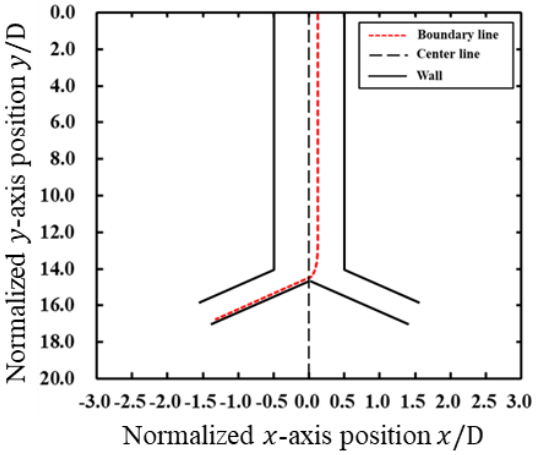

Fig. 12: Boundary line dividing the left-right flow distribution

The boundary line dividing the flow distribution is shown in Figure 12. The horizontal coordinate of the boundary line in the parent branch was $x/D = 0.13$. Figure 13 shows the relationship between particle trajectory and the flow distribution boundary line.

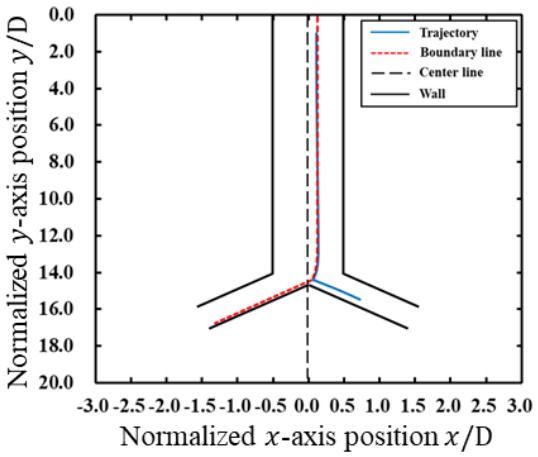

Fig. 13: Particle trajectory and flow distribution boundary line when released from the initial position $(x/D, y/D) = (0.11, 1.0)$

Figure 14 (Appendix) shows the relationship between particle trajectory, the flow distribution boundary line, and the mechanical equilibrium position within the parent branch region. This position is located $1/5$ of the particle diameter to the left of the flow distribution boundary line at $x/D = 0.13$ along the horizontal axis. In this calculation, the Reynolds number was set to $Re = 64$ and the confinement ratio was set to $C = 0.1$.

Figure 14 (Appendix) shows that the particle has crossed the flow distribution boundary line. This was attributed to the particle migration toward the mechanical equilibrium position at $x/D = 0.23$. This suggests that particles may cross the boundary line as a result of migration in an environment where the flow distribution boundary line exists between the initial particle position and the mechanical equilibrium position. Furthermore, when particles cross the boundary line, discrepancies between flow and particle distribution at the bifurcations may occur.

We discuss flow distribution and particle distribution using Figure 15.

In Figure 15, the gray region corresponds to the gray-shaded area in Figure 11(b) (Appendix). This gray region represents the area where particles may cross the boundary line during the migration process toward the mechanical equilibrium position. Under the assumption that particles are uniformly distributed, 13% of the total particles would be located in the gray region. As a result, a 13% discrepancy may occur between the flow rate distribution and the particle distribution at bifurcation.

In the one-way coupling scheme, particle motion strictly obeys streamlines. Therefore, in the one-way coupling scheme, the microscopic particle distribution at the bifurcation completely corresponds to the macroscopic flow rate distribution.

On the other hand, in this study, the two-way coupling scheme was employed to investigate particle behavior, and the results suggested the possibility of a 13% discrepancy between particle distribution and flow rate distribution.

Therefore, under conditions like those in this study, where the particle Reynolds number satisfies $Re_p > 10^{-3}$ and inertial effects must be considered, the relationship between the boundary line and the mechanical equilibrium position can lead to discrepancies between flow rate distribution and particle distribution. This suggests that it is necessary to use a two-way coupling scheme in environments where inertial effects cannot be neglected.

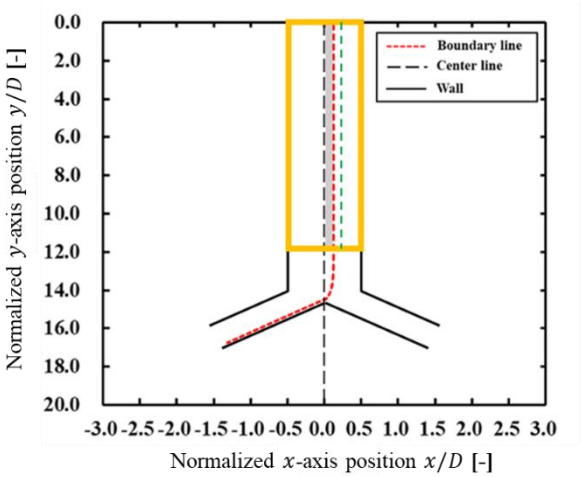

Fig. 15: Relationship between the boundary line and the mechanical equilibrium position

5 Conclusions

In this study, we examined particle behavior under conditions where inertial effects cannot be neglected using a two-dimensional, symmetric bifurcated flow channel. The analysis examined particle behavior in both symmetric and asymmetric flow fields. In a symmetric flow field, the boundary line that

determines which daughter branch the fluid enters corresponds to the centerline of the channel. When a single particle was released from a position left or right of the centerline, the particle migrated away from the centerline. As a result, the possibility of particles crossing the boundary line was considered low. This suggests that, in a symmetric flow field, discrepancies between flow rate distribution and particle distribution at the bifurcation are unlikely to occur. In a flow field where the flow rate was not evenly distributed between the left and right branches, we observed that, under conditions where inertial effects cannot be neglected, depending on the positional relationship between the boundary line and the mechanical equilibrium position, particles crossed the boundary line while migrating toward the equilibrium position.

Furthermore, under the assumption that particles are uniformly distributed, we found that a 13% discrepancy may arise between flow rate distribution and particle distribution at the bifurcation.

Declaration of Generative AI and AI-assisted Technologies in the Writing Process

The authors wrote, reviewed and edited the content as needed and they have not utilized artificial intelligence (AI) tools. The authors take full responsibility for the content of the publication.

References:

[1] World Health Organization, The top 10 causes of death, [Online]. https://www.who.int/news-room/fact-sheets/detail/the-top-10-causes-of-death (Accessed Date: December 17, 2024).

[2] Riva, D. A., Evangelista, C. A., and Puleston, P. F., Efficient Algorithm for Pulmonary Nonlinear Model Online Estimation of Patients Under Assisted Ventilation, *WSEAS Transactions on Biology and Biomedicine*, Vol.20, pp.257-266, 2023. https://doi.org/10.37394/23208.2023.20.27.

[3] Ji, Z., Hao, S., Pang, J., and Ganchev, I., Automatic Pulmonary Nodule Detection and Management System, *WSEAS Transactions on Biology and Biomedicine*, Vol.22, pp.190-199, 2025. https://doi.org/10.37394/23208.2025.22.20.

[4] Zhao, J., Feng, Y., Koshiyama, K., and Wu, H., Prediction of airway deformation effect on pulmonary air-particle dynamics: A numerical study, *Physics of Fluid*, Vol.33, No.10, pp.101906-1-101906-17, 2021 DOI: 10.1063/5.0065309.

[5] Weibel, E. R., Morphometry of the Human Lung, *Springer*, 1963

[6] Islam, Md. R., Larpruenrudee, P., Rahman, Md. M., Cui, X., Mortazavy Beni, H., Inthavong, K., Ullah, S., Godder, T. K., Dong, J., Gu, Y., Islam, Mohammad S., How Nanoparticle Aerosols Transport through Multi-Stenosis Sections of Upper Airways: A CFD-DPM Modelling, *Atmosphere*, Vol.13, No.8, pp.1-22, 2022. DOI: 10.3390/atmos13081192.

[7] Ou, C., Hang, J., Hua, J., Zhao, B., Li, Y., Deng, Q., and Ling, H., Particle Deposition in Large-Scale Human Tracheobronchial Airways Predicted by Single-Path Modelling, *International Journal of Environmental Research and Public Health*, Vol.20, No.5, pp.1-15, 2023. DOI: 10.3390/ijerph20054583.

[8] Ou, C., Hang, J., and Deng, Q., Particle Deposition in Human Lung Airways: Effects of Airflow, Particle Size, and Mechanisms, *Aerosol and Air Quality Research*, Vol. 20, No. 12, pp. 2846–2858, 2020. DOI: 10.4209/aaqr.2020.02.0067.

[9] Islam, M. R., and Feng, Y., Achieving Targeted Delivery of Chemotherapeutic Particles to Small Airway Tumors via Pulmonary Route Using Endotracheal Catheters: A CFPD Study, *Pharmaceuticals*, Vol.16, No.2, pp.1-17, 2023. DOI: 10.3390/ph16020158.

[10] Wang, J., Zhang, Y., Chen, X., Feng, Y., Ren, X., Yang, M., and Ding, T., Targeted delivery of inhalable drug particles in a patient-specific tracheobronchial tree with moderate COVID-19: A numerical study, *Powder Technology*, Vol.405, pp.1-15, 2022. DOI: 10.1016/j.powtec.2022.117520.

[11] Talaat, M., Si, X. A., Dong, H., and Xia, J., Leveraging statistical shape modeling in computational respiratory dynamics: Nanomedicine delivery in remodeled airways, *Computer Methods and Programs in Biomedicine*, Vol.204, pp.1-14, 2021. DOI: 10.1016/j.cmpb.2021.106079.

[12] Rahman, Md. M., Zhao, M., Islam, M. S., Dong, K., and Saha, S. C., Nanoparticle transport and deposition in a heterogeneous human lung airway tree: An efficient one path model for CFD simulations, *European Journal of Pharmaceutical Sciences*, Vol.177, pp.1-13, 2022. 10.1016/j.ejps.2022.106279.

[13] Stickel, J. J., and Powell, R. L., Fluid mechanics and rheology of dense suspensions, *Annual Review of Fluid Mechanics*, Vol.37, pp.129-149, 2005. DOI: 10.1146/annurev.fluid.36.050802.122132.

[14] Segré, G., and Silberberg, A., Radial particle displacements in Poiseuille flow of suspensions, *Nature*, Vol.189, No.4760, pp.209-210, 1961. DOI: 10.1038/189209a0.

[15] Di Carlo, D., Inertial Microfluidics: Mechanisms and Applications, *Lab on a Chip*, Vol.9, No.21, pp.3038-3046, 2009. DOI: 10.1039/b912547g.

[16] Fukui, T., and Kawaguchi, M., Numerical study of microscopic particle arrangement of suspension flow in a narrow channel for the estimation of macroscopic rheological properties, *Advanced Powder Technology*, Vol.33, pp.1-10, 2022. DOI: 10.1016/j.apt.2022.103855.

[17] He, X and L. S. Luo, Lattice Boltzmann model for the incompressible Navier-Stokes equation, *Journal of Statistical Physics*, Vol.88, No.3, pp.927–944, 1997. DOI: 10.1023/B:JOSS.0000015179.12689.e4.

[18] Tanno, I., Morinishi, K., Matsuno, K., and Nishida, H., Validation of virtual flux method for forced convection flow, *JSME International Journal Series B*, Vol.49, No.4, pp.1141-1148, 2006. DOI: 10.1299/jsmeb.49.1141.

[19] Adachi, H., Fukui, T., and Kawaguchi, M., Parallel computing of the high-order virtual flux method coupled with the lattice Boltzmann method for pressure-driven particle-laden flow simulations, *Journal of Fluid Science and Technology*, Vol.19, No.3, pp. 1-15, 2024. DOI: 10.1299/jfst.2024jfst0025.

[20] Inamuro, T., Maeda, K., and Ogino, F., Flow between parallel walls containing the lines of neutrally buoyant circular cylinders, *International Journal of Multiphase Flow*, Vol.26, No.12, pp.1981–2004, 2000. DOI: 10.1016/S0301-9322(00)00007-0.

Contribution of Individual Authors to the Creation of a Scientific Article (Ghostwriting Policy)

- Daisuke Haraguchi, Investigation.
- Tomohiro Fukui, Supervision.

Sources of Funding for Research Presented in a Scientific Article or Scientific Article Itself

This work was supported in part by research grant from Takahashi Industrial and Economic Research Foundation.

Conflict of Interest

The authors have no conflicts of interest to declare.

APPENDIX

Table 1. Conditions for validation of a single particle model in a two-dimensional channel under Poiseuille flow

Calculation area		$x \times y = L_x \times L_y = D \times D$
Resolution		200 cells$/D$
Characteristic velocity		$U = 0.041$
Working fluid density		$\rho = 1.0$
Initial conditions	Pressure	$\frac{\partial p}{\partial x} = -\frac{12\rho U^2}{ReD}$
	Velocity	$u = \frac{1}{2\mu}\frac{\partial p}{\partial x} y(y - D)$
Boundary conditions	Inflow	Periodic boundary condition with pressure difference
	Outflow	Periodic boundary condition with pressure difference

Table 2. Parameters of a single rigid circular particle in a two-dimensional channel at each of the Conditions

	Particle initial position y_0	Reynolds number Re	Confinement C
Condition 1	$0.20, 0.30, 0.40$	27.54	0.25
Condition 2	0.40	$12.73, 27.54, 54.91$	0.25
Condition 3	0.40	27.54	$0.20, 0.25, 0.30$

Table 4. Calculation conditions for verification

Calculation area		$x \times y = L_x \times L_y = D \times D$
Resolution		200 cells$/D$
Characteristic velocity		$U = 0.01$
Reynolda number		$Re = 64$
Working fluid density		$\rho = 1.0$
Confinement		$C = 0.1$
Initial conditions	Pressure	$\frac{\partial p}{\partial x} = -\frac{12\rho U^2}{ReD}$
	Velocity	$u = \frac{1}{2\mu}\frac{\partial p}{\partial x} y(y - D)$
Boundary conditions	Inflow / Outflow	Periodic boundary condition with pressure difference

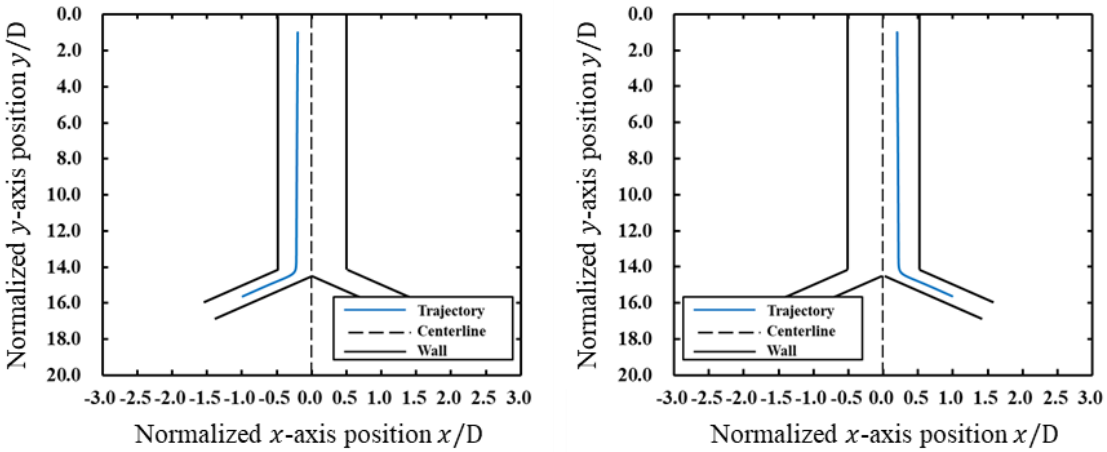

Fig. 8: (a) Particle trajectory when released from the initial position$(x/D, y/D) = (-0.2, 1.0)$. (b) Particle trajectory when released from the initial position $(x/D, y/D) = (0.2, 1.0)$

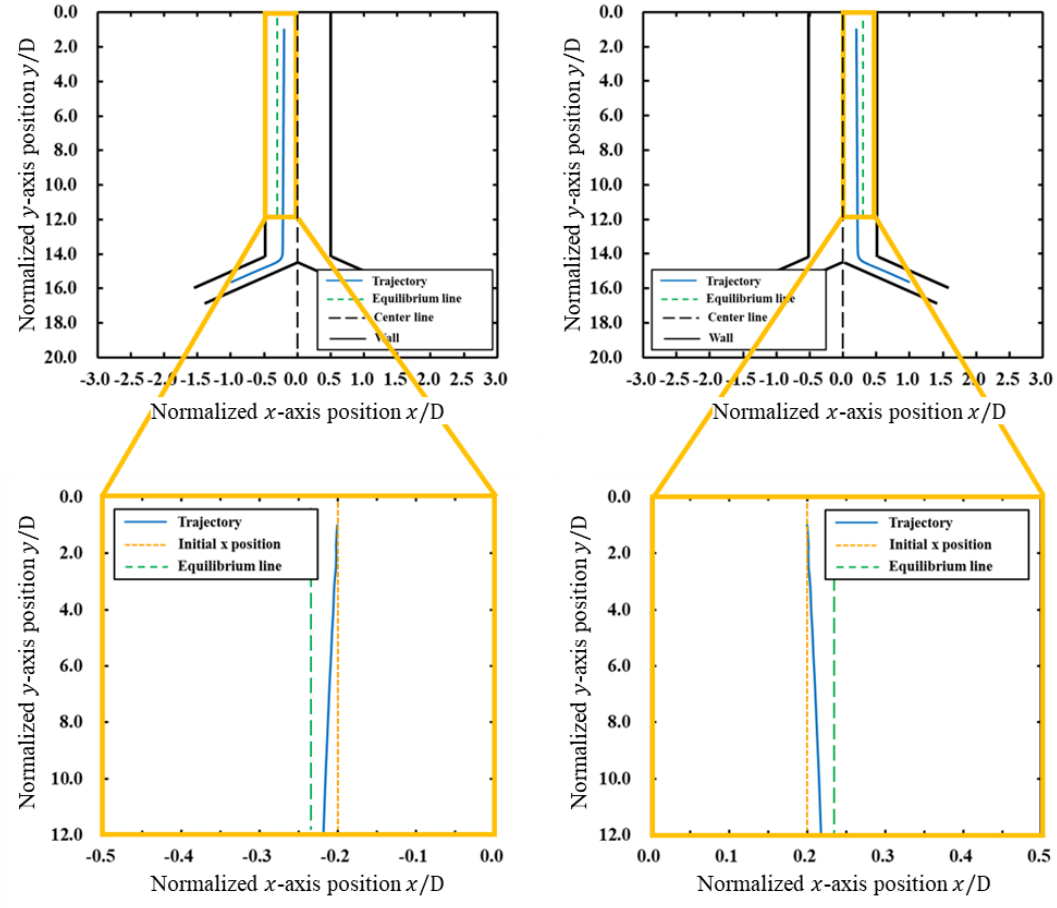

Fig. 9: Horizontally stretched diagram showing the relationship between particle trajectory and mechanical equilibrium line within the parent branch. (a) On the horizontal axis, $x/D = -0.5$ corresponds to the left wall of the parent branch, and $x/D = 0.0$ corresponds to the center of the channel. (b) On the horizontal axis, $x/D = 0.0$ corresponds to the center of the channel, and $x/D = 0.5$ corresponds to the right wall of the parent branch

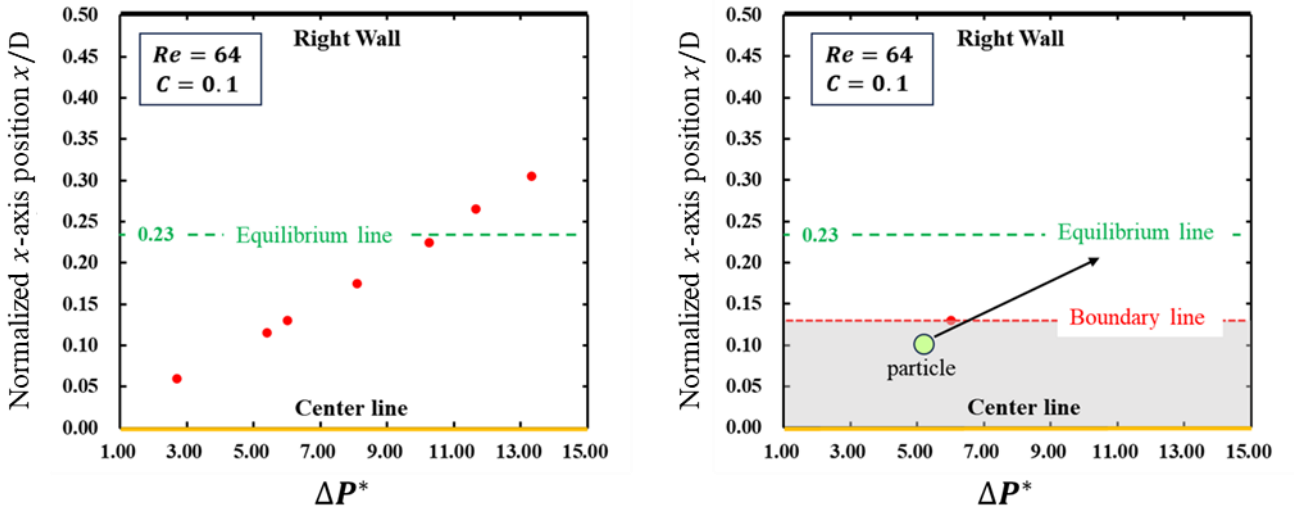

(a) (b)

Fig. 11: (a) Relationship between the normalized outlet pressure difference, the boundary line, and mechanical equilibrium position within the parent branch. (b) Relationship between the boundary line, mechanical equilibrium position, and particle migration

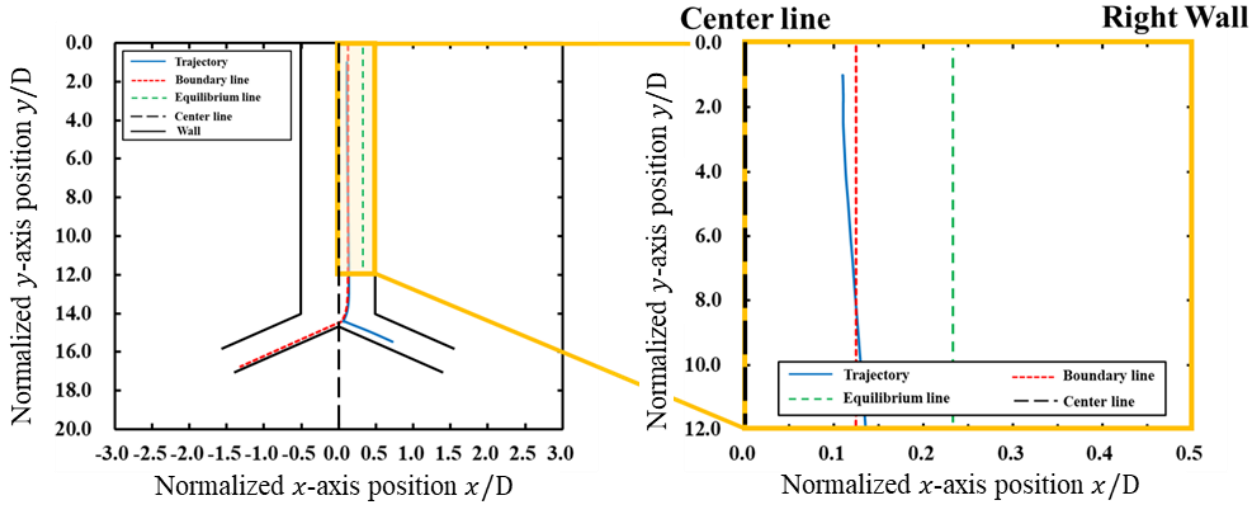

Fig. 14: Horizontally stretched diagram showing the relationship between particle trajectory and mechanical equilibrium line within the parent branch